RSC Advances

ROYAL SOCIETY OF CHEMISTRY

www.rsc.org/advances

In situ formed porous carbon nanofibers by electrospinning with volatile solvent additive into an ice water bath for lithium sulfur batteries

Ling Huang[a,b], Jianli Cheng[b], Guoxing Qu[b], Xiaodong Li[b], Yang Hu[a], Wei Ni[b], Demao Yuan[b], Yun Zhang[a]*, Bin Wang[b]*

[a] College of Materials Science and Engineering, Sichuan University, Chengdu, Sichuan 610065, China.

[b]New Materials R&D Center, Institute of Chemical Materials, China Academy of Engineering Physics, Mianyang, Sichuan 621900,China.

*Address correspondence to binwang@caep.cn; edward.bwang@gmail.com;

Fax: (+86) 816-2544 426.

Abstract

In situ formation of polyacrylonitrile (PAN) nanofibers with porous structure was fabricated by electrospinning ternary PAN/*N*,*N*'-dimethylformamide (DMF)/Chloroform ($CHCl_3$), and ternary PAN/DMF/Tetrahydrofuran (THF) solution systems into a glass dish filled with ice water bath. These porous carbon nanofibers (*p*CNFs) are both mesoporous and microporous with high specific surface area without the requirement of physical or chemical activation, which mainly originated from *in-situ* evaporation of the volatile solvent additive and the dissolution of the solvent in the ice water bath. The synthesis process is simple and versatile. The effects of precursor components, precursor concentration and the collection methods on the morphology and size distribution of fibers have been investigated. The obtained *p*CNFs with porous structure and large surface area were then utilized as conductive matrixes for sulfur (S) to form *p*CNFs/S nanocomposite. Electrochemical measurements show that the *p*CNFs/S nanocomposite can deliver ~400 and ~340 mAh g^{-1} after 50 cycles and 100 cycles at 0.5 C, corresponding to 80.1% and 68% capacity retention with a high Coulombic efficiency, respectively.

Keywords: porous carbon nanofiber (*p*CNFs), *in situ*, electrospinning, lithium sulfur batteries

1. Introduction

Thanks to their high theoretical capacity (1675 mAh/g) and specific energy (2600 Wh/kg with a Li electrode), lithium sulfur (Li/S) batteries have attracted tremendous attention in recent years. Combined with the low cost and nontoxicity of sulfur, Li/S battery has been considered as a promising candidate for next generation energy storage system. [1-5] Unfortunately, several serious problems, including low sulfur utilization, fast capacity fading and poor cycle life, are still big challenges that hinder the application of Li/S batteries. These problems can be traced back to the poor conductivity (the insulating nature of S) of sulfur, the formation of intermediate polysulfides (Li_2S_x, $4 \leq x \leq 8$) that can dissolve into the electrolyte, and large volumetric expansion of sulfur (~80%) during cycling. [3, 6-8]

An attractive approach to enhance the performance of Li/S batteries is constructing porous carbon-S nanocomposites in which sulfur particles are embedded in micro or mesopores of the conductive carbon matrixes.[9-20] On one hand, conductive carbon matrixes can increase the electrical conductivity of the sulfur cathode and also provide fast transport paths for electrons and lithium ions. On the other hand, carbon materials with special porous structure can be ideal absorbents for both active sulfur and the soluble polysulfides, leading to excellent Coulombic efficiency and cycle stability for Li/S batteries. Recently, various carbon materials including microporous carbon spheres,[10] mesoporous carbon nanoparticles,[16] carbon nanofibers (CNFs),[13, 21, 22] and graphene[18, 23] have been synthesized and utilized to encapsulate sulfur successfully. Among them, CNFs with porous or hollow structures have been considered as an attractive matrix for active sulfur with improved electrochemical performance, due to their unique structure in terms of long fiber length and high specific surface area.[11, 13, 24, 25] The porous CNFs (*p*CNFs) can form ideal interwinded reservior-like matrixes for active sulfur. Meanwhile, the porous structure in *p*CNFs can not only confine the active sulfur but also trap the soluble polysulfides, which can greatly reduce the shuttle effect of polysulfide. In addition, their excellent mechanical property, structure integrity, and good conductivity can promote the transfer of lithium ions and electrons, which is a key factor to obtain good electrochemical performance. Typical studies were reported by Ji *et al.*[13] and Guang *et al.*[25], the results demonstrated that *p*CNFs can improve the capacity and stability of Li/S cells by well-confining sulfur into their pores and entrapping the dissolution of polysulfides effectively. However, the fabrication of porous carbon nanofibers often requires a pore-creation step, involving multiple chemical and physical activation reactions, which is complex and costly. An alternative approach to produce porous carbon nanofibers is using templates, which can provide carbon nanofibers with precisely controlled pore sizes. Nevertheless, many technical difficulties such as template design, carbon growth, frame removal, high cost, and scale-up issues are still remained. Thus, developing a facile and inexpensive method to prepare *p*CNFs is strongly desired.

Electrospinning has been widely used as a simple and versatile method to prepare long fibers that can be applied to synthetic and natural polymers, polymer alloys, and polymers/inorganic materials.[26-29] Carbon fibers can be easily

obtained by electrospinning the polymer solution of polyacrylonitrile (PAN), a well-known precursor for carbon fibers, followed by stabilization and carbonization.[30-33] Currently, *p*CNFs are prepared by either adding polymer component additives[30, 32] to the electrospinning solution which act as pore-generators or utilize chemical[34] and physical activation[35, 36] in the subsequent carbonization process. In order to further simplify the fabrication processes for *p*CNFs, we here present the *in situ* formation of *p*CNFs by ice water bath collecting electrospinning with mixed solvent additive followed by carbonization. In this work, tetrahydrofuran (THF) and chloroform ($CHCl_3$) were selected as the volatile solvent to be added to the PAN /dimethylformamide (DMF) solution to form PAN/DMF/THF and PAN/DMF/$CHCl_3$ ternary systems. By collecting the electrospun PAN fibers into an ice water bath, porous texture is formed simultaneously due to the strong phase separation process and the high humidity of the electrospinning environment. The different additives, additive solvent ratios and the collection methods, three main parameters that might influence the surface morphology and size distribution of PAN fibers, are then studied in this work. Furthermore, the obtained *p*CNFs were utilized as a conductive matrix of active S to form *p*CNFs/S nanocomposite, which was used as the cathode for Li/S batteries. The results show that *p*CNFs with high conductivity and large surface area are good matrixes to absorb and disperse sulfur. The *p*CNFs/S nanocomposite can deliver ~400 and ~340 mAh g^{-1} after 50 cycles and 100 cycles at 0.5 C, corresponding to 80.1% and 68% capacity retention, respectively.

2. Experimental section

2.1. Electrospinning processes

In situ formation of porous polymer nanofibers was fabricated by a simple electrospinning method with a glass dish filled with 4 °C ice water bath as the collector. First, PAN (Sigma-Aldrich, Mw = 150,000) was dissolved in DMF at 60 °C with magnetic stirring until complete dissolution. Then $CHCl_3$ or THF was added into the above solution followed by stirring at least 24 h to obtain homogeneous solutions (ternary PAN/DMF/$CHCl_3$ and PAN/DMF/THF solution systems). The solutions were driven from the syringe equipped with a blunt spinneret at a constant rate of 0.5 mL/h by a syringe pump. A high voltage of 15 kV was applied to the blunt spinneret by a high voltage DC power supply. Nanofibers were collected onto a piece of grounded Al foil or into a glass dish filled with 4 °C ice water bath which fixed on a grounded steel plate with a tip-to-collector distance of 15 cm.

2.2. Fabrication of porous carbon nanofibers

As-spun nanofibers were firstly dried in an oven overnight. The obtained PAN nanofibers were then tailored and transferred to a tube furnace and stabilized at 280 °C for 6 h (heating rate was 2 °C min^{-1}) in air atmosphere. In this step, thermoplastic PAN absorbed oxygen from air and converted to a non-plastic cyclic or ladder-like compound, which is a key process for the retention of the fiber morphology in the subsequent carbonization process.[13, 37, 38] Then the stabilized fibers were carbonized at 1000 °C for 8 h (heating rate was 5 °C min^{-1}) in N_2 atmosphere to form porous

carbon nanofibers (*p*CNFs). This procedure allowed the complete carbonization of PAN fibers. During carbonization, non-carbonized components were removed in the form of a variety of gases (e.g., H_2O, N_2, HCN, and CO_2 and others), and carbon content remained to be about 50~57 wt% of the original PAN, thus leading to the decrease of fiber diameter.

2.3. Synthesis of *p*CNFs/S nanocomposite

Firstly, the sublimed sulfur (S) powder (280 mg) was dissolved in carbon disulfide (CS_2) (100 mg/ml). 120 mg *p*CNFs (made from PAN/DMF/THF system) was dispersed in the solution and sonicated for 6 h to form a homogeneous solution. Then magnetic stir was applied to the *p*CNFs/S solution until the CS_2 solvent completely evaporated. The formed *p*CNFs/S precipitate was thermally treated at 155 °C for 12 h under nitrogen flow. In order to further decrease the sulfur content and remove the sulfur at the surface of carbon nanofibers, this sample was further heated at 160 °C for another 6 h in a N_2 atmosphere.

2.4. Materials characterization

The morphologies of the samples were characterized using scanning electron microscopy (SEM, Hitachi S-4800), transmission electron microscopy (TEM, JEOL JEM -100CX operating at 80 kV), and energy dispersive X-ray spectroscopy (EDX). The composition and crystal structures of the samples were obtained by X-ray diffraction analysis (XRD, Bruker-AXS D8 DISCOVER). Thermogravimetric analysis (TGA) was conducted on a TGA 1, STAR^e System (Mettler Toledo) to measure the weight ratio of S in the composite at a heating rate of 10 min^{-1} from 50 °C to 800 °C under nitrogen flow. Nitrogen adsorption and desorption isotherms were carried out at 77 K on a Brunauer-Emmett-Teller surface area analyzer (BK300, Beijing JWGB Sci&Tech Co., Ltd.)

2.5. Electrochemical measurements

The *p*CNFs/S electrode was prepared by mixing the *p*CNFs/S nanocomposite, acetylene black and polyvinylidene fluoride (PVDF) at a weight ratio of 70: 20: 10 in NMP to form homogeneous slurry under magnetic stirring. The slurry was then plastered onto aluminum foil using a doctor blade, and dried at 50 °C for at least 48 h. CR2032-type coin cells were assembled by sandwiching a porous polypropylene separator (Celgard 2400) between the *p*CNFs/S electrode and Li metal foil in a high-purity argon-filled glove box. The electrolyte used was 1 M lithium bis(trifluoromethanesulfonyl)imide (LITFSI) dissolving in a mixture of 1, 2-dimethoxyethane (DME) and 1, 3-dioxolane (DOL) (1:1 in volume). Typical Sulfur loading density in the whole electrode was calculated to be is 0.8~1.2 mg cm^{-2}. Galvanostatic discharge and charge cycling of the Li/S batteries was conducted using the CT2001A battery program controlling test system (China-Land Co., Ltd.) from 1.0 to 3.0 V. Cyclic voltammogram (CV) and electrochemical impedance spectroscopy (EIS) measurements were performed on a VSP (Bio-Logic SAS) electrochemical workstation with a voltage from 1.0 V to 3.0 V versus Li^+/Li and amplitude of 10 mV in the frequency range of 200 KHz to 100 mHz, respectively.

3. Results and discussion

Various parameters such as polymer concentration, solution solvents, collection types, and environmental temperature and humidity can influence the morphology of fibers during the electrospinning processes. Here, in our mixed solvents solution systems, the solvent additive types, the weight ratio of the solvent additives and the collection methods are the main factors that might influence the morphology of the as-spun polymer nanofibers. In order to optimize the synthesis process, we first investigated the effects of the ratios of solvent additives on the morphology of the resultant electrospun fibers. Electrospinning of PAN/DMF, PAN/DMF/1, 3, 5, 7 wt% $CHCl_3$ and PAN/DMF/1, 3, 5, 7 wt% THF was conducted at 8.5 wt% polymer concentration. The corresponding SEM images are given in Fig. 1. Fiber-like textures can be observed in all samples (Fig. 1a-i). When the ratio of solvent additives is low (1wt %), PAN nanofibers have uniform and continuous fiber morphology. The size distribution and the average diameter of the fibers are also measured and summarized in Table1.

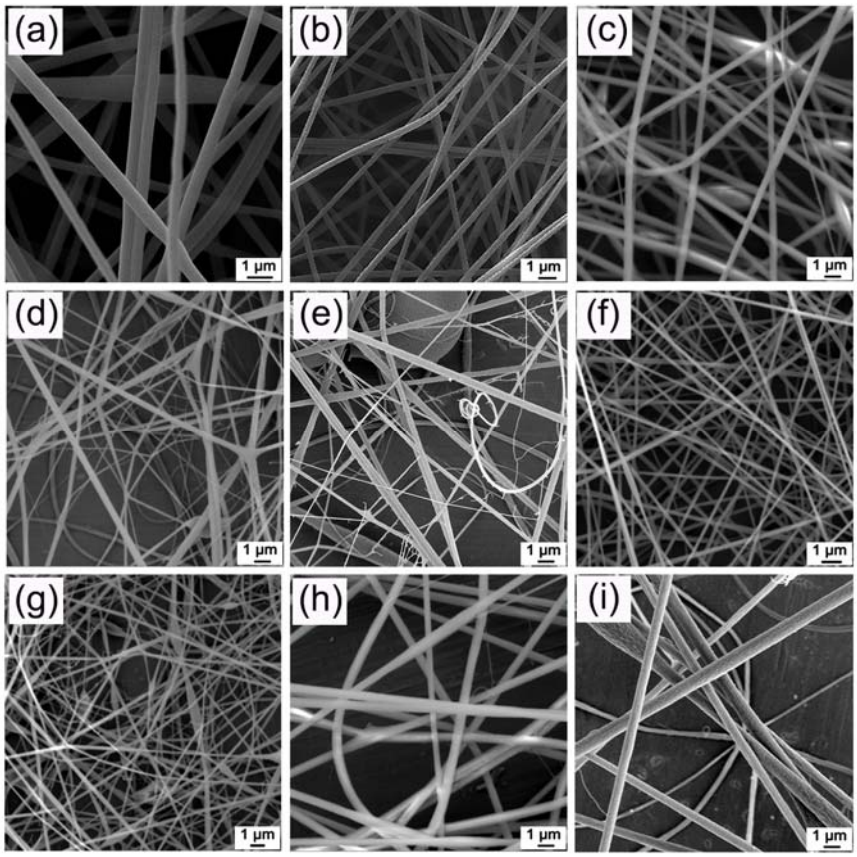

Figure 1. SEM images of PAN fibers prepared from: (a) PAN/DMF solution; (b-e) PAN/DMF/$CHCl_3$ solutions with 1, 3, 5, 7 wt% $CHCl_3$ content, respectively; (f-i) PAN/DMF/THF solutions with 1, 3, 5, 7 wt% THF content in the solution, respectively. The weight percentage of PAN in all samples is 8.5 wt%.

Interestingly, the average fiber diameter is found to decrease from 380 to 320 nm after the introduction of additive solvents and the size distribution of the fibers obtained from PAN/DMF/1wt% $CHCl_3$ or THF are found to be narrower compared with fibers obtained from pure PAN/DMF solution, *i.e.,* 190-590 nm for PAN nanofibers made from PAN/DMF (Fig. 1a), 270-450 nm for PAN nanofibers made from PAN/DMF/1wt% $CHCl_3$ (Fig. 1b), and 200-420nm for PAN nanofibers made from PAN/DMF/1wt% THF (Fig. 1f), respectively. The observed decrease in both the average fiber diameter and the size distribution with adding 1wt% additive solvent could be due to the decrease in the viscosity and the increase in the conductivity of the spinning solutions. However, significant morphological changes are observed with the increase in the concentration of the $CHCl_3$ and THF additives (3，5, and 7 wt%). As it can be seen from Fig. 1 c-e and g-i, it is difficult to obtain homogeneous and continuous fibers when the additive concentration is increased to 3, 5 and 7 wt%. Ultrafine nanofibers with diameters much smaller than that of the majority are occurred, and the PAN nanofibers are composed of a mixture of fibers and beads as well as some clusters. Meanwhile, the size distribution and average fiber diameter of PAN nanofibers electrospinning from these precursors are wider and larger than that obtained from lower additive content (1wt%), as shown in Table 1, indicating that the spinnability of PAN solutions has the tendency to decrease with the increase of $CHCl_3$ and THF contents. This is due to the insolubility of PAN in $CHCl_3$ and THF, which results in low homogeneity of the PAN solution, and consequently the spinnability of PAN precursors deteriorates. Therefore, considering the morphology and size distribution of PAN nanofibers, we choose the PAN/DMF/1wt%$CHCl_3$ and PAN/DMF/1wt%THF solution systems as the precursors.

Table 1. Size distribution and average fiber diameter of polymer fibers electrospinning from different PAN solutions

Composition (8.5wt% PAN/DMF+ CHCl3 (wt%)	THF (wt%)	Size distribution range (nm)	Average fiber diameter (nm)
0	0	190~590	380
1	0	270~450	360
3	0	120~820	490
5	0	130~950	410
7	0	160~1230	590
0	1	200~420	320
0	3	130~610	300
0	5	80~1260	630
0	7	70~910	370

The size distribution of PAN fibers was calculated by counting 50 fibers in the corresponding SEM images (Figure 1) using Nano Measure analysis tool.

The influence of electrospinning collector on the morphology of PAN nanofibers has been further investigated. Fig. 2 shows two fiber collecting methods: (1) collecting onto a piece of grounded Al foil, and (2) collecting directly into a glass dish filled with ice water bath which fixed on a grounded steel plate. The corresponding SEM images of nanofibers collected by both ways are also shown in Fig. 2 a-l. It can be seen that PAN nanofibers made from pure PAN precursor followed by collecting onto Al foil have smooth outer surface and bead-free fibrous morphology (Fig. 2a and b). In contrast, rough surface morphology of the products is observed when the fibers were collected by ice water bath during the electrospinning process (Fig. 2c and d). For PAN/DMF/1wt%$CHCl_3$ system where $CHCl_3$ is introduced, the SEM images of nanofibers are showed in Fig. 2e-h. Instead of smooth surface morphology made from pure PAN precursor, rough and bumpier surface morphology of fibers can be observed when collected by Al plate collector (Fig. 2e and f). More interestingly, nano-pores are formed on the fiber surface when the ice water bath was used as the collector (Fig. 2g and h). Similar morphology changes are also observed in the PAN/DMF/1wt%THF system, as shown in Fig. 2i-l. PAN fibers with rough and bumpier outer surface morphology can be obtained when collected by Al plate collector (Fig. 2i and j), while numerous nano-pores and ultrafine crackles are visible on the fiber surface using the ice water bath collector (Fig. 2k and l).

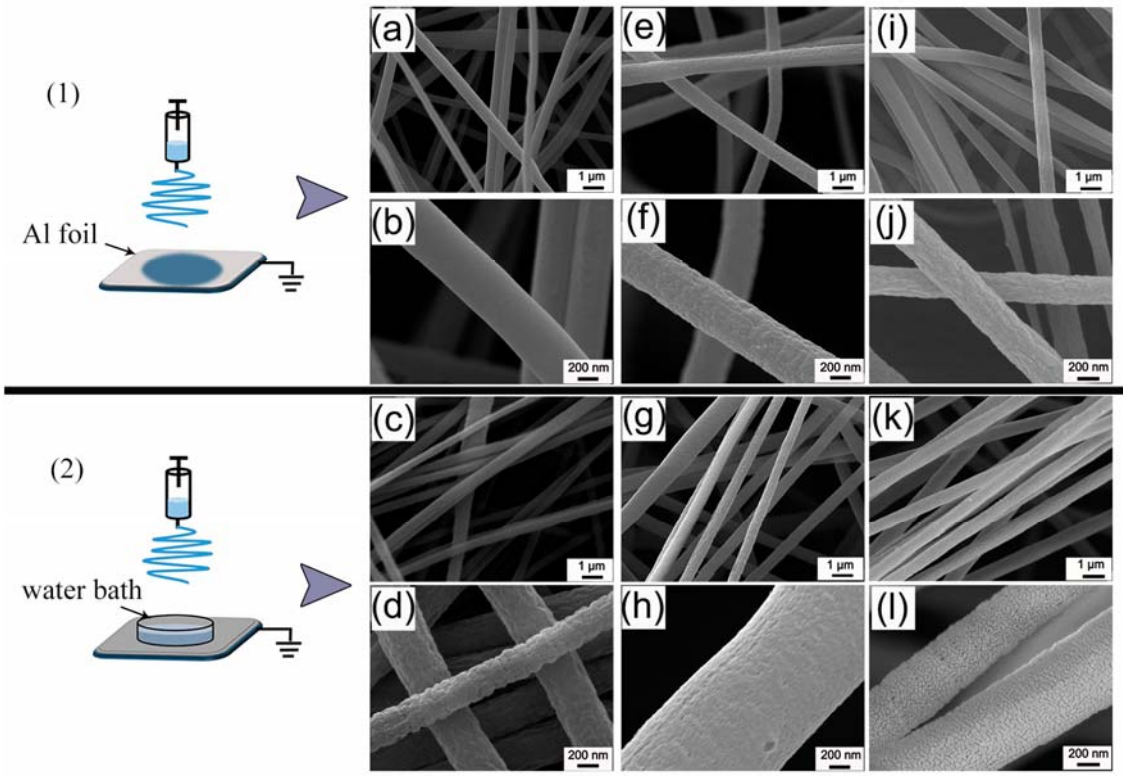

Figure 2. The electrospinning setup with (1) a piece of grounded Al foil; (2) a glass dish filled with 4 °C water bath as the collector in these experiments, the rest of the setup are similar to those reported in literatures. SEM images of PAN

nanofibers electrospinning from: (a-d) 8.5wt%PAN/DMF solution, (e-h) 8.5wt% PAN/DMF/1wt% $CHCl_3$ solution, (i-l) 8.5wt% PAN/DMF/1wt%THFsolution. PAN nanofibers in (a,b,e,f,i,j) are collected by (1) a piece of grounded Al foil; PAN nanofibers in (c,d,g,h,k,l) are collected by (2) a glass dish filled with 4 °C water bath.

Therefore, it is clear that the ice water bath can influence the surface morphology of the electrospinning nanofibers. Meanwhile, nano-pores as well as ultrafine crackles cannot form *in situ* on the surface of polymer fibers during the electrospinning procedure unless a solvent additive (*i.e.,* $CHCl_3$ or THF) and water bath collector are combined. Such phenomenon can be assigned to the classical phase-separation principle and the effect of humidity.[36, 39] During the electrospinning process, the occurrence of phase separation leads to the formation of two new phases: PAN-rich phase and PAN-deficient phase. The PAN-rich phase rapidly solidifies to form the fiber matrix when the solvent evaporates. In the case of PAN/DMF system, because of the low vapor pressure of DMF, the cooling effect, which generated from the evaporation of DMF, has failed to create pores. Even by collecting the electrospinning fibers into an ice water bath, which has greatly increased the humidity of the electrospinning environment, rough surface instead of pores is observed on the surface of PAN fibers, indicating that the dissolution of DMF and water condensation on the surface of fibers, if happened, are not sufficient to leave pores due to the low volatility of DMF solvent. Therefore, two volatile solvents ($CHCl_3$ or THF) were selected and added in order to improve the volatility of the precursor solution, which is a critical factor for the formation of porous texture. Coupled with the high humidity provided by the low temperature water bath in the electrospinning environment, the phase separation processes take place in a strong degree, which is beneficial for the generation of porous structure. It should be noted that numerous crackles are also found on the surface of PAN nanofibers derived from the PAN/DMF/THF ternary system. We speculate that the crackles are generated by rapid phase separation during electrospinning and the subsequent dissolution of residual THF in H_2O, as soon as the fibers dropped into the water bath collector.

A typical heat treatment process of pre-oxidation and carbonization is then conducted to convert electrospun PAN nanofibers into CNFs. The surface morphology of CNFs is characterized by SEM (Fig. 3e, f, g, h, i, j) and TEM (Fig. 3k and l). It can be seen that the obtained carbon nanofibers display uniform fibrous morphologies with homogenously distributed diameters, similar with the as-spun polymer fibers (Fig. 3a-d). The average diameters of as-spun PAN nanofibers made from PAN/DMF/1wt%$CHCl_3$ (Fig. 3a and b) and PAN/DMF/1wt%THF (Fig. 3c and d) are ~340 and ~320 nm, respectively, while their carbonized nanofibers have a smaller diameter around 240 nm, suggesting substantial shrinkage during the heat treatment process. After carbonization, nanofibers appear to be broken into short fibers, as shown in Fig. 3e-j. While CNFs derived from PAN/DMF solution (Fig. 3e and f) and PAN/DMF/1wt% $CHCl_3$ (Fig. 3g and h) show very similar fiber morphologies, the morphology of CNFs obtained from PAN/DMF/1wt%THF (Fig. 3i and j) is quite different, as shown in Fig. 3j. Pores and crackles are maintained on the

surface of the carbon nanofibers. Besides, the cross section displays that porous structure is crossing the whole fiber. In order to further investigate the morphology differences of these samples, TEM images of CNFs are also displayed in Fig. 3 k and l. In the TEM images, nano-pores are still maintained after the transformation processes from PAN phase to carbon during heat treatment, which means that the *in situ* formed porous structures would not influence by the subsequent heating process. However, as it can be seen from Fig. 3k, porous structure is only formed on the surface of *p*CNFs that obtained from PAN/DMF/1wt%$CHCl_3$, while distinct porous structure crossing the whole carbon nanofibers is obtained from PAN/DMF/1wt%THF (Fig. 3l).

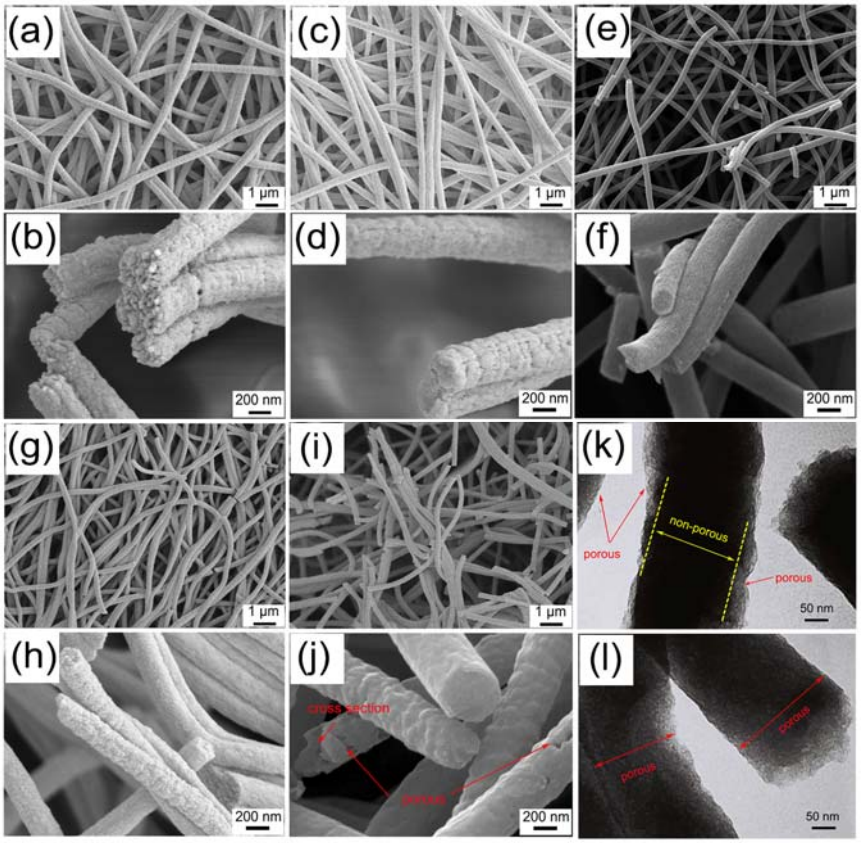

Figure 3. SEM images of the as-spun porous PAN nanofibers which derived from (a, b) PAN/DMF/1wt%$CHCl_3$ ternary system, and (c, d) PAN/DMF/1wt%THF ternary system, respectively; SEM images of carbon nanofibers obtained from: (e, f) PAN/DMF precursor, (g, h) PAN/DMF/1wt%$CHCl_3$, and (i, j) PAN/DMF/1wt%THF precursor solution; (k) and (l) TEM image of porous carbon nanofibers (*p*CNFs) corresponding to the SEM images shown in (g, h) and (i, j), respecitively.

The specific surface area and pore volume of *p*CNFs prepared from PAN/DMF, PAN/DMF/1wt%$CHCl_3$, and PAN/DMF/1wt%THF precursors are analyzed by the nitrogen adsorption-desorption isothermal at 77 K, and the results

are summarized in Table 2. It can be seen that carbon nanofibers made from ternary solution precursors (PAN/DMF/1wt%$CHCl_3$ and PAN/DMF/1wt%THF) mainly have mesoporous structure and exhibit specific surface areas of 31.8 and 136.2 $m^2 g^{-1}$, respectively. This is higher than the surface area (20.3 $m^2 g^{-1}$) of non-porous nanofibers prepared from pure PAN precursor (0 wt% additives). In the meantime, both micropore and mesopore volumes of *p*CNFs obtained from PAN/DMF/1wt%THF are higher than those of *p*CNFs from PAN/DMF/1wt%$CHCl_3$ precursor. This result is consistent with that of the SEM and TEM images in Fig. 2 and Fig. 3, demonstrating that THF is a better additive solvent candidate for constructing porous carbon nanofiber architecture due to its high volatility and solubility in water.

Table 2. Specific surface, pore volume and pore size of CNFs prepared from PAN/DMF, PAN/DMF/1wt%$CHCl_3$ and PAN/DMF/1wt%THF

Content PAN/DMF with different additive content	[a]SSA ($m^2 g^{-1}$)	[b]TPV ($cm^3 g^{-1}$)	[c]V_{meso} ($cm^3 g^{-1}$)	[d]V_{micro} ($cm^3 g^{-1}$)	Average pore diameter(nm)
0	20.3	0.0084	0.0067	0.0017	8.0
1wt% $CHCl_3$	31.8	0.07	0.056	0.014	9.3
1wt% THF	136.2	0.48	0.453	0.026	14.2

[a]SSA: specific surface area; [b]TPV: total pore volume; [c]V_{meso} : mesopore volume; [d]V_{micro}:micropore volume

As has been mentioned, carbonaceous with porous structure are widely used as hosts or absorbents for sulfur to achieve improved electrochemical performance because of their good conductivity and high specific surface area. Based on this, we selected the *p*CNFs with higher specific surface area that derived from PAN/DMF/1wt%THF solution system as a possible matrix to encapsulate active sulfur into the pores of *p*CNFs *via* a simple sulfur sublimation method. The as-prepared *p*CNFs/S nanocomposite displays a non-uniform surface morphology with the occurrence of many short fibers, as shown in Fig. 4a. The average diameter of such *p*CNFs/S nanocomposite is measured to be ~244 nm, which is very similar to that of the pure *p*CNFs before sulfur filling (around 240 nm, Fig. 3h and i), indicating that most of the sulfur have been well encapsulated by the *p*CNFs matrix. High magnification image in Fig. 4b shows that the surface morphology of *p*CNFs/S nanocomposite becomes smoother than that of the pure *p*CNFs (Fig. 3i and j), further demonstrating that the porous channel of *p*CNFs has been well filled with S. No obvious surface deposition and aggregation of sulfur are found in the *p*CNFs web. The inset in Fig. 4b is the EDX spectrum of *p*CNFs/S nanocomposite, which reveals clearly C peak and S peak. Fig. 4c presents the XRD patterns of *p*CNFs/S nanocomposite, *p*CNFs, and pure S. *p*CNFs shows one characteristic graphite peak. The broad and low-intensity peak

indicates that the as-formed *p*CNFs have an amorphous structure with a low degree of graphitization, which could be attributed to the low carbonization temperature (1000 °C) compared to the typical graphitization temperature of 2800 °C.[40] While sharp diffraction peaks observed in the XRD patterns of both pure S and *p*CNFs/S nanocomposite denote that sulfur exists in a crystalline state, which are completely different from the XRD pattern of pure *p*CNFs and all the peaks are consistent with the peaks of standard orthorhombic structure of S_8 (JCPDS, PDF#08-0247). The sulfur content in the *p*CNFs structure is determined from the TGA curves (Fig. 4d), demonstrating that 67.4 wt% sulfur is incorporated in the *p*CNFs/S nanocomposite.

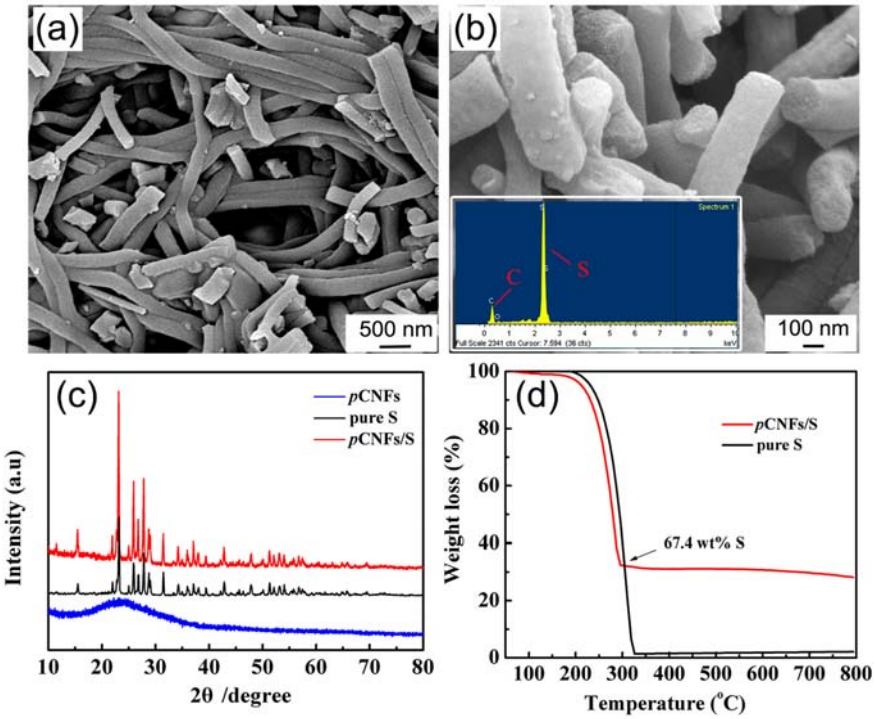

Figure 4. SEM images of the prepared *p*CNFs/S nanocomposite (a) and (b), the inset image in (b) is the EDS spectrum of the *p*CNFs/S nanocomposite. (c) XRD patterns of the *p*CNFs, *p*CNFs/S nanocomposites and pure S. (d) TGA curves of pure S and *p*CNFs/S nanocomposites.

Electrochemical performance of the above *p*CNFs/S nanocomposite is further investigated in a Li/S battery system. CR2032-type coin cell is assembled using the *p*CNFs/S nanocomposites as cathode materials and lithium foils as anode materials. Fig. 5a presents the cyclic voltammogram (CV) curves of the *p*CNFs/S electrode. During the initial cathodic process of the composite, two main reduction peaks appear at around 2.2 V and 2.0 V (vs. Li/Li^+), respectively, which can be assigned to the two-step reduction mechanism of sulfur with metal Li.[19, 41] In these potential stages, sulfur would react with Li and produce a series of lithium polysulfides (Li_2S_x, $1 \leqslant x \leqslant 8$). A weak cathodic peak located at ~1.56 V is also observed in the first cycle, as shown in the inset image. This reduction peak should be assigned to the reaction

between the insoluble Li_2S_2 and Li_2S.[42] In the first anodic scan, a broad peak is observed in the potential of approximately 2.65 V, which is attributed to the conversion of Li_2S into high-order soluble polysulfides.[13] In the subsequent five cycles, the reduction peaks are located at about 2.24 V and 1.75V, and the oxidation peak shows at a lower potential of approximately 2.54V, indicating a good reversibility with cycling. The decrease of intensity in the subsequent cycles and peak shift may be associated with the irreversibility of the low-order lithium polysulfide conversion process.

Fig. 5b illustrates the 1st and 2nd discharge/charge profiles of the *p*CNFs/S electrode at a current rate of 0.02 C between 1.0 and 3.0 V. Two typical characteristic plateaus are observed in the discharge curves, which resulted from the two-step discharge mechanism of S with Li metal, consisting with the CV result.[13, 19, 41] An initial discharge capacity of 1155 mAh g^{-1} at 0.02 C is obtained while only 886.1 mAh g^{-1} discharge capacity maintained in the 2nd cycle. There is a short potential plateau at ~1.56 V in the first discharge curve, which agrees well with the CV analysis (inset in Fig. 5a). The short potential plateau indicates the existence of a small amount of elemental sulfur, which may be not encapsulated by the porous carbon nanofibers, that is, sulfur is attached on the surface of carbon nanofibers. The generated polysulfides from the sulfur on the outer surface and in the pore of the nanofibers during discharge process would partially dissolve in the electrolyte and further react with Li to form insoluble Li_2S_2 and Li_2S, thus leading to the loss of active sulfur and the irreversible capacity loss. This is also demonstrated by the low Coulombic efficiency (84.7%) that observed in the first cycle. In the second cycle, the plateau at ~1.56 V can hardly be distinguished, and the Coulombic efficiency increases markedly from 84.7% to 97.7%. The excellent Coulombic efficiency observed in the 2nd cycle demonstrates that sulfur and the polysulfides are well constrained by the *p*CNFs absorbent. In comparison, two electrodes with lower sulfur content were also fabricated by immersing the above electrode (67.4 wt% sulfur content) into CS_2 for 1 and 2 minutes followed by washing with ethanol for three times, respectively. Actually, in the washing process, we found it is quite difficult to control the conditions to ensure the complete removal of sulfur on the outer surface of carbon nanofibers. Thus, sulfur content in the composite would decrease in comparison with the previous one before washing step. After this process, the sulfur contents in the electrodes are measured to be about 59.2 wt% and 46.7 wt%, suggesting that sulfur attached on the outer surface of carbon fibers and a portion of sulfur that encapsulated in the carbon nanopores have been removed. The change of sulfur content would also change the electrochemical properties of the *p*CNFs/S electrode. The initial discharge and charge capacity of the electrode with 59.2 wt% sulfur content are 1034.7 mAh g^{-1} and 946.6 mA h g^{-1}, corresponding to a Coulombic efficiency of ~91.5 %, higher than that observed in the previous electrode before washing (84.7%, Fig. 5b). Similar initial charge-discharge efficiency (91.6%) is obtained for the electrode with reduced sulfur content of 46.7 wt%. The improvement of the initial Coulombic efficiency further demonstrates that the *p*CNFs/S electrodes exhibit a good reversibility and the

dissolution of polysulfides during the first discharge process can be well suppressed by washing off the residual sulfur on the outer surface of carbon matrix.

When Li/S cell is charged/discharged at various current rates from 0.02 C to 2 C, the *p*CNFs/S electrode can deliver 886.1, 645.9, 529.6, 430.2, and 353.8 mAh g^{-1} at 0.02, 0.05, 0.1, 0.2, and 0.5 C, respectively (Fig. 5c and d). Even at a high current rate of 2 C, a capacity of *ca.* 280 mAh g^{-1} can be obtained, showing a good rate capability. Cycling performance of the *p*CNFs/S electrode is also investigated at the corresponding current rate of 0.5 C.

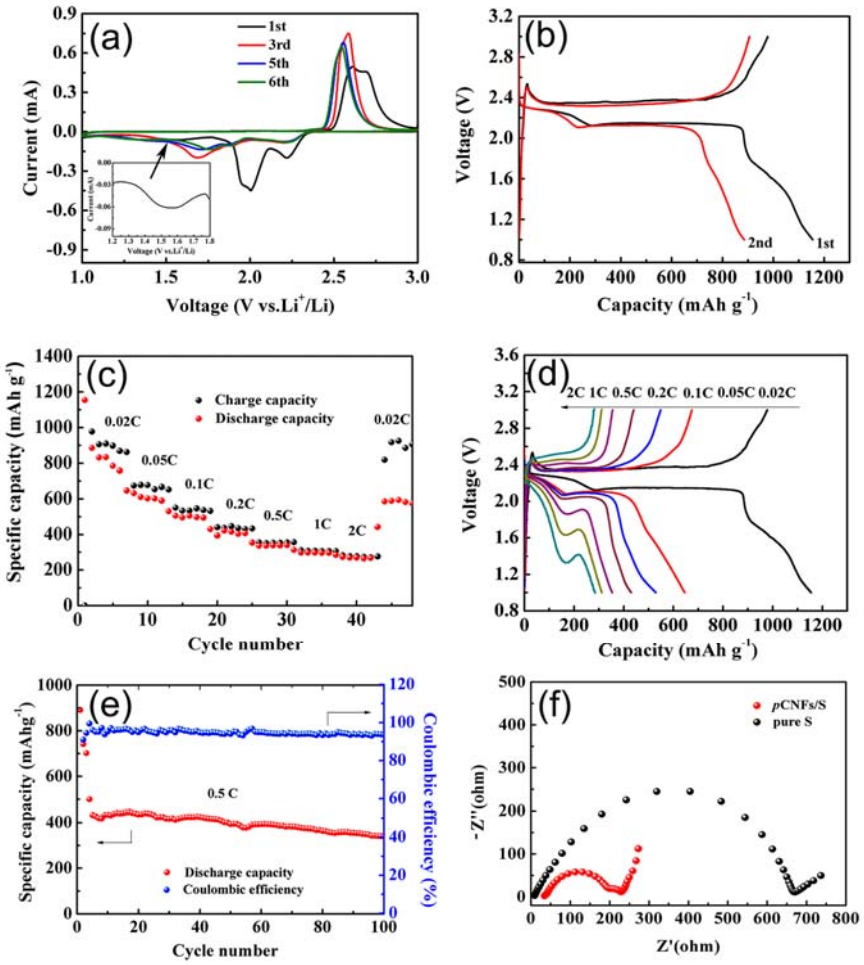

Figure 5. (a) CV curve of the *p*CNFs/S composite electrode at a scanning rate of 0.1 mV s^{-1} in the voltage window from 1.0 to 3.0 V, inset is the magnified image of the first cycle. (b) The 1st and 2nd galvanostatic charge/discharge profiles of the *p*CNFs/S electrode; (c) rate capability for the *p*CNFs/S nanocomposite electrode; (d) the corresponding voltage profile of the *p*CNFs/S nanocomposite electrode at different current rates; (e) Cycling performance of the *p*CNFs/S electrode at a constant rate of 0.5 C; (f) EIS spectra of pure S and the *p*CNFs/S electrode before cycling.

In Fig. 5e, after the initial three activation at 0.02 C, a discharge capacity of ~500 mAh g^{-1} is measured at 0.5 C with a Coulombic efficiency of approximately 100%. The *p*CNFs/S nanocomposite electrode displays a good reversibility with a discharge capacity of ~400 and ~340 mAh g^{-1} after 50 cycles and 100 cycles, corresponding to 80.1% and 68% capacity retention, respectively. Meanwhile, as high as 93.4% of the Coulombic efficiency can still maintain after 100 cycles. Fig. 5f shows the EIS spectra of the pure S electrode and the *p*CNFs/S electrode before cycling. The depressed semicircle in the high frequency region is assigned to the charge-transfer resistance (Rct). The inclined line in the low frequency region represents the Warburg impedance (W_o), which is related to solid-state diffusion of lithium-ions into the electrode material. The charge transfer resistance of the *p*CNFs/S electrode is about 197.9 Ω, much smaller than that of the pure S electrode (662.6 Ω), indicating that charge transport at the *p*CNFs/S/electrolyte interface is much easier compared to that at the pure S/electrolyte interface. This result demonstrates that *p*CNFs are good reservoirs for sulfur.

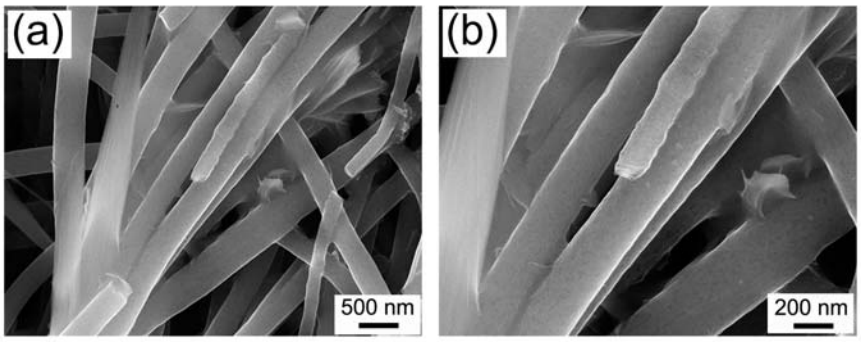

Figure 6. SEM images of a *p*CNFs/S composite electrode after 100 charge/discharge cycles at a current rate of 0.5 C.

In order to further investigate the function of *p*CNFs in the electrode, the morphology and structural changes of the *p*CNFs/S composite electrodes after charged/discharged at a constant current rate of 0.5 C for 100 cycles are also explored. The coin cell was disassembled and characterized by SEM, as shown in Fig. 6. Comparing with SEM images before cycling (Fig. 4a and b), it can be clearly seen that the original nanofibrous morphologies were retained after cycling, revealing that the carbon matrix can maintain the electrode integrity. Because of the strong volatility of the solvent additives and the high humidity of the electrospinning environment, the designed two solvents electrospinning system combined with ice water bath collector can facilitate phase separation during electrospinning process, ensuring that micropore and mesopore structures can be formed *in situ* on the fibers. So improved electrochemical performance can be obtained by constraining sulfur in these pores of the *p*CNFs/S nanocomposites.

4. Conclusions

In summary, we have successfully synthesized *p*CNFs *via* a simple and convenient electrospinning method, which combines the *in-situ* pore-generating processes of volatile solvent additive and ice water bath collector. This method is

much simple and cost effective compared to the conventional method where pore activation agents or pore-generating templates are often required. These *p*CNFs are utilized to encapsulate sulfur to form *p*CNFs/S nanocomposites. The electrochemical results show that *p*CNFs with porous structure and large surface area are good matrixes to constrain the sulfur. The *p*CNFs/S nanocomposites can deliver ~400 and ~340 mAh g^{-1} after 50 cycles and 100 cycles, corresponding to 80.1% and 68% capacity retention, respectively.

Acknowledgements

This work was supported by the Startup Foundation of China Academy of Engineering Physics, Institute of Chemical Materials (KJCX201301 and KJCX201306), National Natural Science Foundation of China (No. 21401177 and 51403193), the "1000 plan" from the Chinese Government, and the R&D Foundation of China Academy of Engineering Physics (2014B0302036).

Notes and references:

1 P. G. Bruce, S. A. Freunberger, L. J. Hardwick and J. M. Tarascon, *Nat. Mater.*, 2012, **11**, 19.

2 A. Manthiram, Y. Fu and Y.-S. Su, *Acc. Chem. Res.*, 2012, **46**, 1125.

3 Y. Yang, G. Zheng and Y. Cui, *Chem. Soc. Rev.*, 2013, **42**, 3018.

4 D. Bresser, S. Passerini and B. Scrosati, *Chem. Commun.*, 2013, **49**, 10545.

5 X. Ji and L. F. Nazar, *J. Mater. Chem.*, 2010, **20**, 9821.

6 S.-E. Cheon, K.-S. Ko, J.-H. Cho, S.-W. Kim, E.-Y. Chin and H.-T. Kim, *J. Electrochem. Soc.*, 2003, **150**, A796.

7 R. D. Rauh, F. S. Shuker, J. M. Marston and S. B. Brummer, *J. Inorg. Nucl. Chem.*, 1977, **39**, 1761.

8 Y. V. Mikhaylik and J. R. Akridge, *J. Electrochem. Soc.*, 2004, **151**, A1969.

9 X. Ji, K. T. Lee and L. F. Nazar, *Nat. Mater.*, 2009, **8**, 500.

10 B. Zhang, X. Qin, G. R. Li and X. P. Gao, *Energy Environ. Sci.*, 2010, **3**, 1531.

11 G. Zheng, Y. Yang, J. J. Cha, S. S. Hong and Y. Cui, *Nano Lett.*, 2011, **11**, 4462.

12 X. Li, Y. Cao, W. Qi, L. V. Saraf, J. Xiao, Z. Nie, J. Mietek, J.-G. Zhang, B. Schwenzer and J. Liu, *J. Mater. Chem.*, 2011, **21**, 16603.

13 L. Ji, M. Rao, S. Aloni, L. Wang, E. J. Cairns and Y. Zhang, *Energy Environ. Sci.*, 2011, **4**, 5053.

14 N. Jayaprakash, J. Shen, S. S. Moganty, A. Corona and L. A. Archer, *Angew. Chem. Int. Ed.*, 2011, **50**, 5904.

15 Y. S. Su and A. Manthiram, *Nat. Commun.*, 2012, **3**, 1166.

16 J. Schuster, G. He, B. Mandlmeier, T. Yim, K. T. Lee, T. Bein and L. F. Nazar, *Angew. Chem. Int. Ed.*, 2012, **51**, 3591.

17 C. Zhang, H. B. Wu, C. Yuan, Z. Guo and X. W. D. Lou, *Angew. Chem. Int. Ed.*, 2012, **124**, 9730.

18 J.-Q. Huang, X.-F. Liu, Q. Zhang, C.-M. Chen, M.-Q. Zhao, S.-M. Zhang, W. Zhu, W.-Z. Qian and F. Wei, *Nano Energy*, 2013, **2**, 314.

19 G. Xu, B. Ding, P. Nie, L. Shen, H. Dou and X. Zhang, *ACS Appl Mater Interfaces*, 2014, **6**, 194.

20 K. Xi, S. Cao, X. Peng, C. Ducati, R. V. Kumar and A. K. Cheetham, *Chem. Commun.*, 2013, **49**, 2192.

21 Q. Li, Z. Zhang, Z. Guo, Y. Lai, K. Zhang and J. Li, *Carbon*, 2014, **78**, 1.

22 Q. Li, Z. Zhang, K. Zhang, J. Fang, Y. Lai and J. Li, *J. Power Sources*, 2014, **256**, 137.

23 H. Wang, Y. Yang, Y. Liang, J. T. Robinson, Y. Li, A. Jackson, Y. Cui and H. Dai, *Nano Lett.*, 2011, **11**, 2644.

24 J. Yang, J. Xie, X. Zhou, Y. Zou, J. Tang, S. Wang, F. Chen and L. Wang, *J. Phys. Chem. C*, 2014, **118**, 1800.

25 G. He, B. Mandlmeier, J. Schuster, L. F. Nazar and T. Bein, *Chem. Mater.*, 2014, **26**, 3879.

26 S. Fukushima, Y. Karube and H. Kawakami, *Polym. J.*, 2010, **42**, 514.

27 A. Greiner and J. H. Wendorff, *Angew. Chem. Int. Ed.*, 2007, **46**, 5670.

28 D. Li, J. T. McCann, Y. Xia and M. Marquez, *J. Am. Ceram. Soc.*, 2006, **89**, 1861.

29 S. Agarwal, A. Greiner and J. H. Wendorff, *Prog. Polym. Sci.*, 2013, **38**, 963.

30 L. Zhang and Y.-L. Hsieh, *Eur. Polym. J.*, 2009, **45**, 47.

31 C. Kim, Y. I. Jeong, B. T. Ngoc, K. S. Yang, M. Kojima, Y. A. Kim, M. Endo and J. W. Lee, *Small*, 2007, **3**, 91.

32 L. Ji, Z. Lin, A. J. Medford and X. Zhang, *Carbon*, 2009, **47**, 3346.

33 H. Niu, J. Zhang, Z. Xie, X. Wang and T. Lin, *Carbon*, 2011, **49**, 2380.

34 Y. S. Yun, C. Im, H. H. Park, I. Hwang, Y. Tak and H.-J. Jin, *J. Power Sources*, 2013, **234**, 285.

35 S.-H. Park, B.-K. Kim and W.-J. Lee, *J. Power Sources*, 2013, **239**, 122.

36 M. Bognitzki, W. Czado, T. Frese, A. Schaper, M. Hellwig, M. Steinhart, A. Greiner and J. H. Wendorff, *Adv. Mater.*, 2001, **13**, 70.

37 S. K. Nataraj, K. S. Yang and T. M. Aminabhavi, *Prog. Polym. Sci.*, 2012, **37**, 487.

38 C. Song, T. Wang, Y. Qiu, J. Qiu and H. Cheng, *J Porous Mater*, 2009, **16**, 197.

39 S. Megelski, J. S. Stephens, D. B. Chase and J. F. Rabolt, *Macromolecules*, 2002, **35**, 8456.

40 A. Oberlin, *Carbon*, 1984, **22**, 521.

41 J. Shim, K. A. Striebel and E. J. Cairns, *J. Electrochem. Soc.*, 2002, **149**, A1321.

42 S. S. Zhang, *Electrochim. Acta*, 2012, **70**, 344.